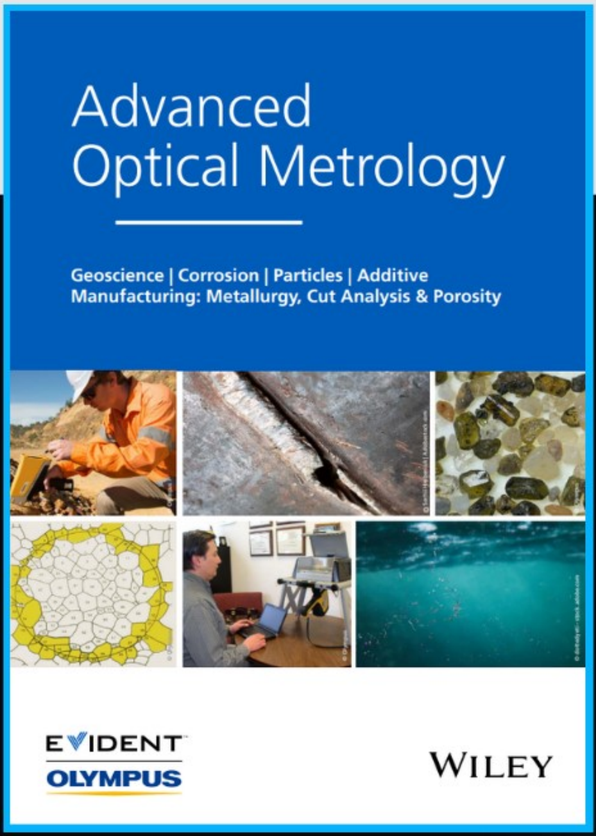

ADVANCED FUNCTIONAL MATERIALS
www.afm-journal.de

Reconstruction of Electric Double Layer for Long-Life Aqueous Zinc Metal Batteries

Yang Yang, Haiming Hua, Zeheng Lv, Minghao Zhang, Chaoyue Liu, Zhipeng Wen, Haodong Xie, Weidong He,* Jinbao Zhao,* and Cheng Chao Li**

Aqueous rechargeable Zn metal batteries (AZMBs) have attracted widespread attention due to their intrinsic high volumetric capacity and low cost. However, the unstable Zn/electrolyte interface causes Zn dendrite growth and side reactions, resulting in poor Coulombic efficiency and unsatisfactory lifespan. Herein, a SiO_2 reinforced-sodium alginate (SA) hybrid film is designed to regulate solid–liquid interaction energy and spatial distribution of all species in the electric double layer (EDL) near the Zn electrode. The unique interfacial layer gives rise to a uniform distribution of Zn^{2+} in the Helmholtz layer through solvation sheath modulation. Moreover, theoretical calculations show that the SO_4^{2-} anions and free-water are substantially reduced in the Helmholtz layer, effectively suppressing hydrogen evolution reaction and formation of by-products through strong charge repulsion and hydrogen bond fixing of free-water. The reconfigured EDL not only ensures homogenous and fast Zn^{2+} transport kinetics for dendrite-free Zn deposition, but also eliminates interface parasitic side reactions. The Zn@SiO_2-SA electrode enables excellent cycling stability of symmetrical cells and high-loading full AZMBs with a lifespan over 3000 h and an areal capacity of 2.05 mAh cm^{-2}, thus laying a solid basis for realizing practical AZMBs.

1. Introduction

With the frequent occurrence of catastrophic accidents involving lithium-ion batteries (LIBs) such as the battery fire of Boeing 787 airplane in 2013, the explosion of Samsung Note 7 phone in 2016, and the spontaneous combustion of Tesla Model S electric vehicle in 2019, battery safety has caused worldwide concern.[1] Most safety hazards of LIBs are closely associated with the flammable and toxic nature of organic electrolytes. Recently emerging aqueous rechargeable battery technologies with the characteristics of inherent safety, low cost, and high ionic conductivity afford a promising alternative solution.[2] Among them, aqueous zinc metal batteries (AZMBs) have been regarded as one of the most promising candidates due to the unique merits of Zn metal anode, including large theoretical capacity (820 mAh g^{-1} and 5851 mAh mL^{-1}), low redox potential (–0.763 V vs SHE) and high natural abundance.[3] However, the issues of Zn dendrites and undesired side reactions during cycling result in low Coulombic efficiency (CE) and poor cycle life, impeding their further progress.[4]

The interface between metallic Zn and aqueous electrolyte essentially determines how Zn^{2+} ions are plated and stripped from the electrode, but is thermodynamically unstable in water.[5,6] Current efforts to stabilize the Zn interface have mainly focused on liquid electrolyte optimization and electrode coatings. Regulating the solvation sheath structure with highly concentrated electrolytes and functional additives can decrease H_2O molecules around Zn^{2+} ions, and reduce H_2O-induced passivation and corrosion reactions.[7–11] Surface modification is also proposed to reduce the direct contact between electrode and electrolyte, and mechanically suppress dendrites.[12–38] However, interfacial issues on the Zn metal anode are rather complex, these reported protection approaches often fail to achieve uniform ion distribution, high Zn^{2+} transfer number and good mechanical strength compatibly, leading to the limited improvement at high-rate or high-capacity cycling conditions.

Efforts through Zn interface chemistry are proposed. It is generally accepted that the inner layer of electric double layer (EDL) nearest to the Zn electrode consists of water molecules

Y. Yang, H. Hua, Z. Lv, M. Zhang, C. Liu, J. Zhao
State Key Lab of Physical Chemistry of Solid Surfaces
State-Province Joint Engineering Laboratory of Power Source Technology for New Energy Vehicle
College of Chemistry and Chemical Engineering
Xiamen University
Xiamen 361005, P. R. China
E-mail: yangyang419@xmu.edu.cn; jbzhao@xmu.edu.cn

Z. Wen, C. C. Li
School of Chemical Engineering and Light Industry
Guangdong University of Technology
Guangzhou 510006, P. R. China
E-mail: licc@gdut.edu.cn

H. Xie, W. He
National Key Laboratory of Science and Technology on Advanced Composites in Special Environments
Center for Composite Materials and Structures
Harbin Institute of Technology
Harbin 150080, P. R. China
E-mail: weidong.he@hit.edu.cn

The ORCID identification number(s) for the author(s) of this article can be found under https://doi.org/10.1002/adfm.202212446.

DOI: 10.1002/adfm.202212446

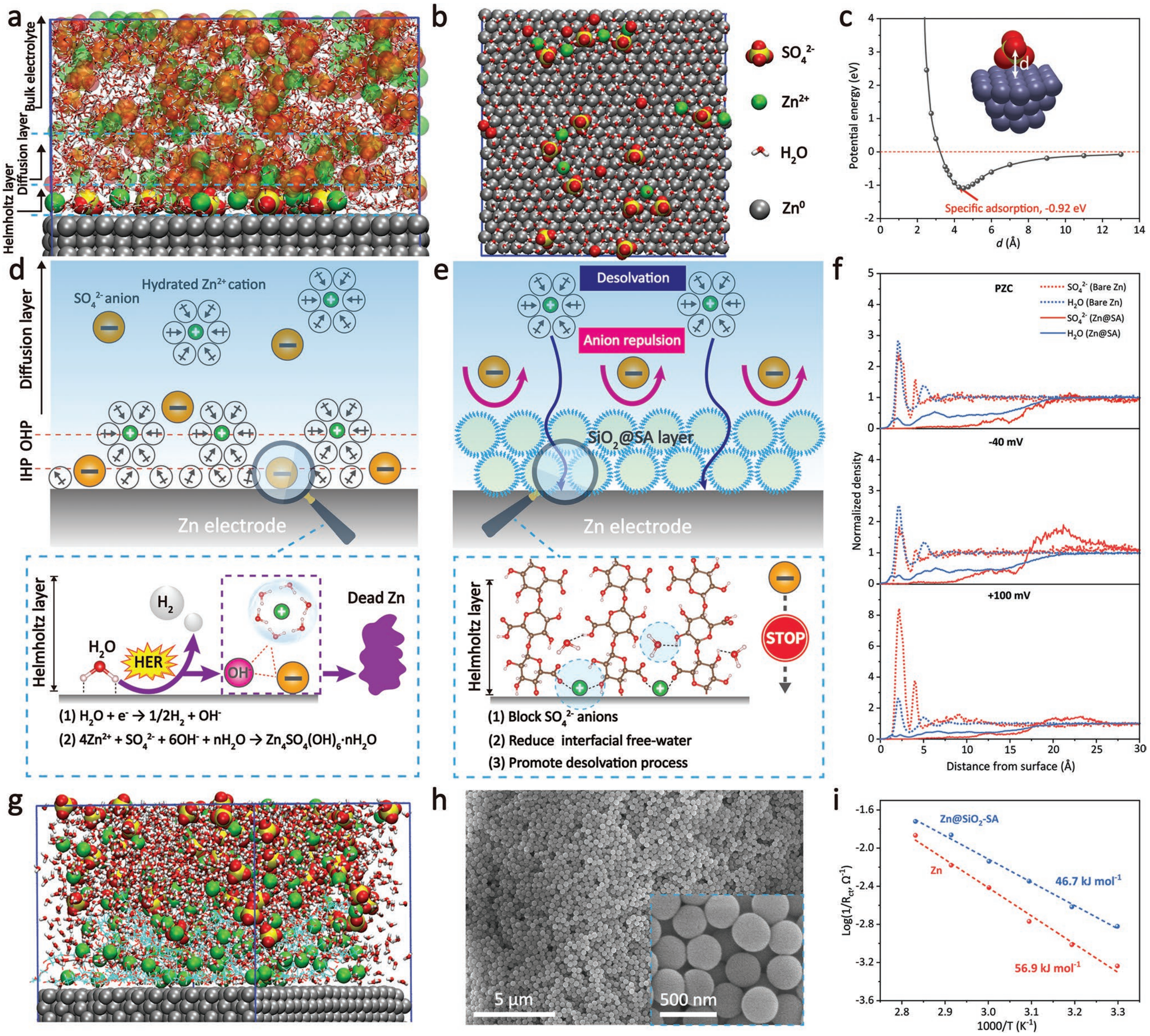

Figure 1. a) The snapshot of EDL structure for Zn metal interface in 2 M $ZnSO_4$ aqueous solution at the PZC through MD simulations (the Helmholtz layer region is highlighted). b) The cross-sectional image of simulated Helmholtz region. c) Potential energy curve of SO_4^{2-} on Zn metal [001] surface in SMD water solvent environment. Schematic illustrations of the EDL structure for d) bare Zn and e) Zn@SiO_2-SA electrode. f) Normalized density profiles of SO_4^{2-} ions and H_2O for Zn metal surfaces with/without SA at various potentials. g) Image snapshots of Zn@SA interfaces through MD simulations. h) SEM image of the Zn@SiO_2-SA electrode. i) Temperature dependencies of charge-transfer resistances of bare Zn and Zn@SiO_2-SA electrodes.

(Figure S3, Supporting Information), which is called the inner Helmholtz plane (IHP).[26,39] The hydrated Zn^{2+} ions cannot pass through water molecules and remain in the second layer, which is defined as the outer Helmholtz plane (OHP). In such a simplified Gouy–Chapman–Stern model of EDL, the existence and influence of anions in the Helmholtz layer are overlooked, resulting in ineffective control over the interface chemistry of the Zn anode and the short lifetime of AZMBs.

In this work, molecule dynamics (MD) simulations of Zn metal in conventional $ZnSO_4$ aqueous electrolyte (2 M) are conducted to gain clear understanding on the EDL structure. The snapshot of simulated EDL structure at the potential of zero charge (PZC) is shown in **Figure 1**a, and the cross-sectional image of Helmholtz layer region is plotted in Figure 1b. In addition to Zn^{2+} cations and water molecules, a large amount of SO_4^{2-} anions are also observed in the Helmholtz layer since SO_4^{2-} anions tend to be adsorbed on the Zn metal surface to reduce the total surface free-energy, as confirmed by the high binding energy between Zn and SO_4^{2-} (Figure 1c). The normalized density profile of the Helmholtz layer (Figure S4, Supporting Information) illustrates that the closest distance between H_2O, SO_4^{2-} and Zn metal surface is 2.1 Å, which is smaller than that between Zn^{2+} and electrode surface (≈2.7 Å). Based on the simulation results, we propose a precise EDL structure model which is similar to the modified Bockris-Devanathan-Müller model.[40,41] As depicted in Figure 1d, the IHP is composed of water dipoles and SO_4^{2-} anions. Hydrated Zn^{2+} ions can only approach OHP, accompanied with some SO_4^{2-} anions for maintaining charge electric neutrality. Interfacial parasitic side reactions (inset in Figure 1d) are attributed to the existence of rich free-water and non-negligible SO_4^{2-} anions in the IHP. Despite the relatively high hydrogen overpotential for Zn, hydrogen evolution reaction (HER) is unavoidable from the view of thermodynamics due to the low oxidation-reduction potential of Zn/Zn^{2+} couples. Particularly, the high desolvation penalties of hydrated $Zn^{2+}(H_2O)_6$ in OHP cause local polarization and trigger HER of free water in IHP. HER not only accelerates the corrosion rate, but also produces fatal OH^- at the IHP. The generated OH^- rapidly reacts with SO_4^{2-} at IHP to form $Zn_4SO_4(OH)_6 \cdot xH_2O$ by-products (so-called "dead Zn"). From the theoretical point of view, regulating the Helmholtz layer on the Zn metal anode is the ultimate route to suppressing dendrite growth and interfacial parasitic side reactions.[42–44]

We then propose an EDL reconfiguration strategy by coating a SiO_2-sodium alginate (SA) hybrid film onto the Zn metal surface (Zn@SiO_2-SA), to manipulate the distribution and chemical environment of Zn^{2+}, SO_4^{2-} and H_2O in the Helmholtz layer simultaneously (Figure 1e). The SiO_2-SA inorganic/organic interface design integrates their respective superiorities of high mechanical strength and rich functional groups to suppress Zn dendrite growth without compromising beneficial chemical characteristics. Abundant negatively charged carboxylic groups in SA not only exclude negatively charged SO_4^{2-} ions from the Helmholtz layer, but also modulate the solvation sheath environment of positively charged hydrated Zn^{2+} ions and reduce the Zn^{2+} charge-transfer energy barrier from 56.9 to 46.7 kJ mol^{-1} through the preferred coordination between carboxylic oxygen and Zn^{2+}. Meanwhile, the ratio of free-water constituent in the EDL is confirmed to be substantially reduced from 57.3% to 17.5% by DFT calculations due to the hydrogen bond interaction between hydroxyl groups and H_2O molecules. Through manipulating the main driving force (desolvation penalty) and reactant (free-water and SO_4^{2-}) synergistically (inset in Figure 1e), interfacial parasitic side reactions are expected to be effectively inhibited.

2. Results and Discussion

The influence of SA polymeric chains on EDL structures at various potentials is investigated by MD simulations. For the snapshot of Zn interface with SA (Zn@SA) at the PZC (corresponding to the uncharged state), SO_4^{2-} anions in the EDL (with the range of $0 < x < 12$ Å) are substantially eliminated (Figure 1g). Furthermore, the normalized density profiles are also shown in Figure 1f for quantitative interpretation. It is obvious that the peak intensity of H_2O in the EDL of Zn@SA is much lower than that of bare Zn. Besides, the peak intensity of SO_4^{2-} in the EDL of Zn@SA is decreased to almost zero, verifying the excellent charge repulsion effect between SA and SO_4^{2-}. For the EDL of bare Zn at −40 mV (corresponding to the Zn plating process), SO_4^{2-} is only slightly reduced compared to that at PZC, not completely removed (Figure 1f; Figure S5a,b, Supporting Information). The trend of specific adsorption for these SO_4^{2-} anions is relatively strong, which compromises the electrostatic repulsive forces induced by the negatively charged Zn metal surface. However, the presence of SO_4^{2-} in the EDL of Zn@SA at −40 mV is still hardly detected. At +100 mV (corresponding to the Zn stripping process), the net positive charge on bare Zn metal surface results in the dramatic accumulation of SO_4^{2-} anions in the EDL (Figure 1f; Figure S5c,d, Supporting Information). In contrast, the amount of SO_4^{2-} anions in the EDL of Zn@SA remains close to zero, implying that the electrostatic repulsion between SA and SO_4^{2-} is strong enough to resist the Coulombic attraction between SO_4^{2-} and positively charged Zn metal surface. This function of excluding SO_4^{2-} anions is further examined at the larger polarization potentials of −100 and +200 mV (Figures S6 and S7, Supporting Information), verifying the charge repulsion effect of SA in a practical battery system.

To validate the effectiveness of SA preliminarily, the SA film is uniformly coated onto the surface of Zn foil to prepare the Zn@SA electrode (Figure S8a, Supporting Information). Although the cycle life of Zn@SA symmetric cell (973 h) is prominently longer than that of bare Zn (Figure S8b, Supporting Information), Zn dendrites are still found to penetrate the polymer film after cycling owing to the insufficient mechanical strength of the SA layer (Figure S9, Supporting Information). Therefore, we design an organic/inorganic hybrid film to achieve excellent mechanical properties and functional chemical effects simultaneously. In such a rational architecture, high Young's modulus SiO_2 nanospheres with a diameter of ≈300 nm build up a homogenous and robust framework. The strip tensile strength test shows that the tensile breaking stress of SiO_2@SA film (3.737 N) is larger than that of SA film (2.717 N), indicating the enhanced mechanical strength (Figure S10, Supporting Information). Flexible SA molecules are absorbed on the surface of SiO_2 through hydrogen bond interaction (Figure S11, Supporting Information) to serve as the binder and form a continuous polymeric network (Figure 1h). The thickness of SiO_2-SA film is 14.5 µm with high conformity (Figure S12, Supporting Information). In addition, the interfacial properties of the SiO_2-SA film are also systematically examined to probe the influence of reconfigured EDL structure on electrode kinetics. The Zn@SiO_2-SA electrode shows a much smaller contact angle of nearly 0° compared with bare Zn (80.0°), demonstrating that the SiO_2-SA film is easily wetted with aqueous electrolyte to reduce the internal resistance of the cell (Figure S13, Supporting Information). The Zn^{2+} charge-transfer activation energy (E_a) at different interphases is also measured through temperature-dependent EIS of symmetrical cells based on the Arrhenius law (Figure S14 and Table S2, Supporting Information). As shown in Figure 1i, E_a of the Zn@SiO_2-SA electrode (46.7 kJ mol^{-1}) is significantly reduced compared with that of the bare Zn electrode (56.9 kJ mol^{-1}). After the incorporation of SiO_2-SA coating layer, Zn^{2+} transference number ($t_{Zn^{2+}}$) is also notably enhanced from 0.370 (Table S3, Supporting Information) to 0.710 (Figure S15, Supporting Information). The synergistic improvement of interfacial wettability, desolvation process and Zn^{2+} transference number leads to fast Zn^{2+} charge-transfer kinetics on the Zn@SiO_2-SA electrode.

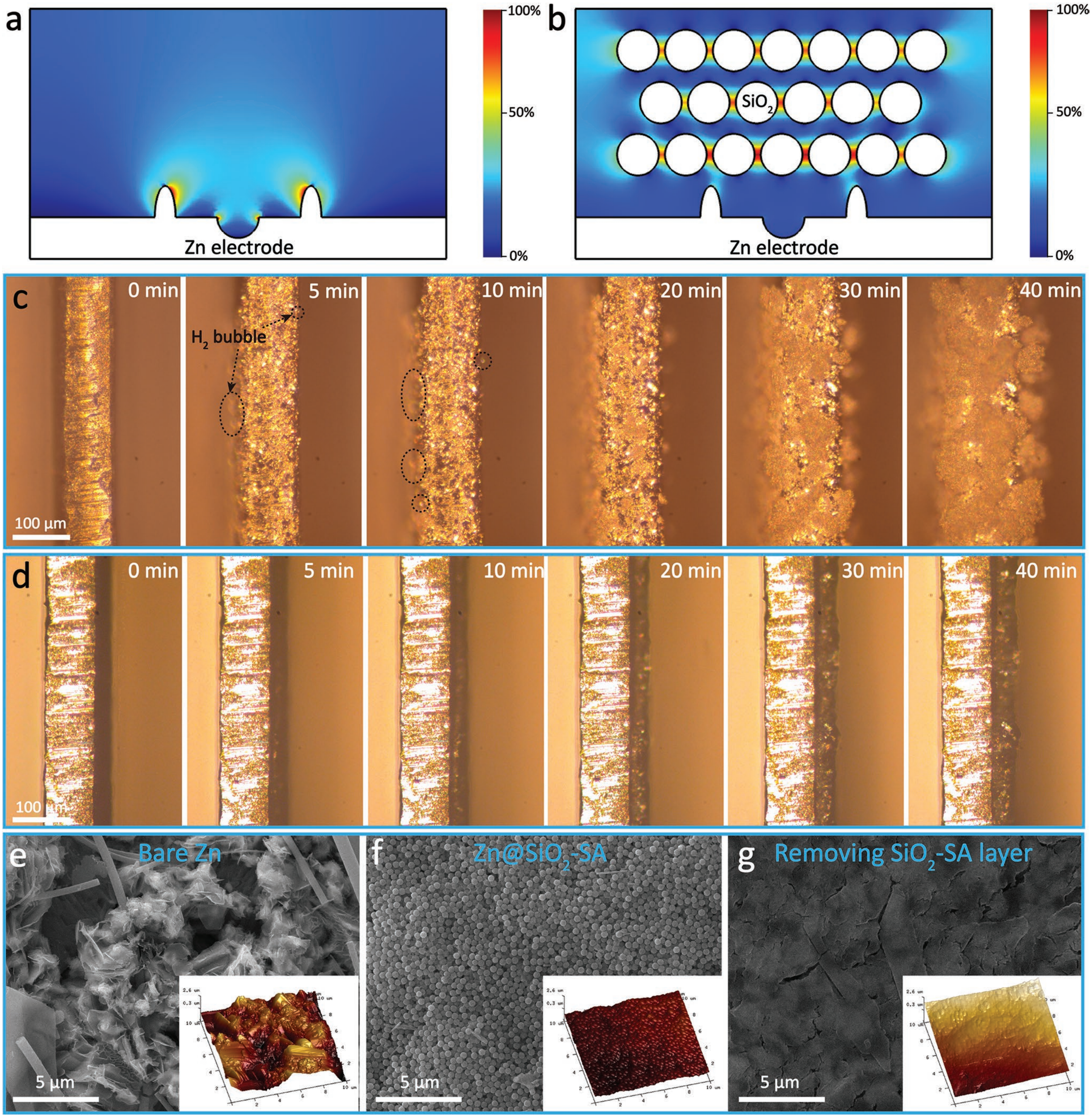

Figure 2. COMSOL simulations of the Zn^{2+} flux on a) bare Zn and b) the Zn@SiO_2-SA electrode. Photographs of c) bare Zn and d) the Zn@SiO_2-SA electrode after different Zn deposition durations of 0, 5, 10, 20, 30, and 40 min at the current density of 10 mA cm^{-2}. SEM images of e) bare Zn, f) the Zn@SiO_2-SA electrode and g) the Zn@SiO_2-SA electrode removing SiO_2-SA layer after 100 cycles at 1 mA cm^{-2} for 1 mAh cm^{-2} (insets are AFM images with the same height scale of –2.0 to 2.6 µm).

The distribution of Zn^{2+} ion is simulated by COMSOL Multiphysics (**Figure 2**a,b). The Zn^{2+}-flux near microscopic pits and protrusions of bare Zn is drastically enhanced (Figure 2a), resulting in "hot spots" for the growth of dendritic Zn. For the Zn@SiO_2-SA electrode (Figure 2b), Zn^{2+} ions are concentrated in the gaps between SiO_2 particles. Furthermore, the reaction interface exhibits excellent homogeneity of Zn^{2+}-flux through the ion redistribution effect of the SiO_2-SA film, contributing to the uniform deposition of Zn metal. *In-situ* optical microscopy of Zn plating behavior on both electrodes is obtained at a current density of 10 mA cm^{-2} (Figure 2c,d). Quite uneven mossy-like Zn deposits are detected after plating for only 5 min on bare Zn, uninterruptedly growing and accumulating into extensive dendrites (Figure 2c; Video S1, Supporting Information). In addition, many gas bubbles resulting from the HER side reactions also occur continuously near the edge of the Zn electrode during the Zn electroplating process. For the Zn@SiO_2-SA electrode (Figure 2d; Video S2, Supporting Information), dense and uniform Zn deposition behavior without any visible gas bubbles is achieved during the entire deposition duration of 40 min. There are inhomogenous and ultrathin hexagonal platelets on the bare Zn electrode after 100 cycles (Figure 2e). In comparison, the surface morphology of the Zn@SiO_2-SA electrode after cycling well retains its original state before cycling with no obvious cracks and dendritic Zn detected (Figure 2f). For the XPS of Zn@SiO_2-SA electrodes before and after cycling (Figure S16, Supporting Information), the characteristic peaks of Si-O bond (103.2 eV) in SiO_2 and C-C/H (284.4 eV), C-O (286.4 eV) and C=O (288.2 eV) bonds in SA molecules are all detected without noticeable shift, demonstrating the excellent chemical stability of SiO_2-SA organic/inorganic hybrid film during repeated cycling. After removing the SiO_2-SA layer, the Zn deposition morphology is also flat and compact (Figure 2g), implying that planar Zn plating/stripping is well confined underneath the SiO_2-SA coating layer. More significant differences can be also reflected in corresponding AFM images (insets in Figure 2e–g). The sharp contrast of roughness reflects the homogeneity of Zn electrodeposition in the Zn@SiO_2-SA electrode, where the SiO_2-SA film evidently regulates the EDL to guide the uniform distribution of electric field and ion flux.

The prepared Zn@SiO_2-SA electrode is then tested in half and symmetric cells to further evaluate its electrochemical performances. At a moderate current density of 2 mA cm^{-2} and a cycling capacity of 1 mAh cm^{-2}, the Zn//Zn symmetric cell owns a higher voltage hysteresis of ≈65.9 mV and short-circuits after only 115 h (**Figure 3**a). In contrast, the Zn@SiO_2-SA cell exhibits an extraordinarily long cycle life of over 3000 h with a small and stable voltage hysteresis of ≈47.6 mV. The cross-sectional SEM image of bare Zn electrode after 100 cycles exhibits porous microstructure with severe agglomeration (inset in Figure 3a), indicating the irreversible consumption of Zn during cycling. The cross-section image of Zn@SiO_2-SA electrode after cycling shows that Zn deposition is uniform and smooth, and the SiO_2-SA film remains intact. As shown in Figure 3b, the XRD pattern of bare Zn after cycling presents two strong peaks at 16.2° and 24.4°, corresponding to the by-product of $ZnSO_4 \cdot 3Zn(OH)_2 \cdot 5H_2O$. In comparison, these peaks are hard to be detected in the Zn@SiO_2-SA electrode after cycling. Even cycled at an extremely high current density of 20 mA cm^{-2}, the Zn@SiO_2-SA symmetric cell still delivers excellent cycling stability (≈2350 h) against bare Zn (Figure 3c). Impressively, an unprecedented, ultra-high cumulative capacity of 47000 mAh cm^{-2} is realized for the Zn@SiO_2-SA electrode (Figure 3e). Besides, the stable cycling performance for a high capacity of 2 mAh cm^{-2} at 5 mA cm^{-2} is also achieved (Figure S17, Supporting Information).

As shown in Figure 3d, the average CE of the Cu@SiO_2-SA||Zn half-cell is as high as 99.8% over 2000 cycles at 2 mA cm^{-2} with a fixed plating capacity of 1 mAh cm^{-2}. In contrast, the CE of the Cu||Zn half-cell fluctuates dramatically after only 155 cycles, which is a direct indicator of internal short-circuit. Moreover, the voltage hysteresis of the Cu||Zn half-cell dramatically increases from 63.5 to 108.7 mV after 150 cycles, which is attributed to the unstable electrochemical interface and the accumulation of dead Zn during repeated cycling (inset in Figure 3d; Figure S18, Supporting Information). However, the voltage hysteresis of the Cu@SiO_2-SA||Zn half-cell maintains below 68.2 mV, and voltage profiles almost overlap throughout 2000 cycles, implying the excellent stability of the electrochemical interface induced by the SiO_2-SA coating layer. Moreover, the CE of the Cu@SiO_2-SA||Zn half-cell at a higher current density of 5 mA cm^{-2} was also investigated (Figure S19, Supporting Information). In particular, the symmetrical cells of Zn@SiO_2-SA electrodes with much thinner SiO_2-SA interfacial layers (2 and 7 µm, Figure S20, Supporting Information) still exhibit improved cycling stability compared with bare Zn, verifying that the enhanced electrochemical performance is resulted from the EDL configuration (Figure S21, Supporting Information).

For practical applications of the Zn@SiO_2-SA anode, zinc metal full battery test is conducted with either MnO_2 or V_2O_5 as the cathode. The MnO_2//Zn@SiO_2-SA cell exhibits outstanding cycling stability with a largely retained capacity of 150.5 mAh g^{-1} after 600 cycles at 1 A g^{-1} (Figure S22a,b, Supporting Information). Moreover, the rate performances of the MnO_2//Zn@SiO_2-SA cell are also improved as compared to the MnO_2//Zn cell (Figure S22c, Supporting Information). Although excellent cycling performance has been achieved for the MnO_2//Zn@SiO_2-SA battery design, it is still difficult to realize high areal capacity AZMBs for practical applications (>2 mAh cm^{-2}) owing to the inherent sluggish electrode kinetics of MnO_2 cathodes. Therefore, a high-loading V_2O_5 cathode (loading mass ≈ 6.5 mg cm^{-2}) with the fast Zn^{2+} diffusion coefficient is also adopted to assemble a full AZMB. The batteries are cycled at a high current density of 7.5 A g^{-1} (corresponding to ≈48.75 mA cm^{-2} at the anode side), which is generally accepted to be an aggressive current as the degradation of Zn metal is accelerated (Figure 3f). The capacity of the V_2O_5//Zn cell decays abruptly after 450 cycles with dramatical fluctuation of CEs, implying the unstable electrochemical interface. In contrast, the initial areal specific capacity of V_2O_5//Zn@SiO_2-SA cell reaches as high as 2.05 mAh cm^{-2}. A much higher capacity of 275.7 mAh g^{-1} with an average capacity decay rate of only 0.0079% per cycle is achieved over 1500 cycles (Figure S23, Supporting Information). Remarkably, the V_2O_5//Zn@SiO_2-SA battery design significantly outperforms most previously reported configurations of AZMBs based on the overall electrochemical performances including areal capacity, lifespan and cycling stability (Figure 3g; Table S4, Supporting Information).[12,13,16,22,29,31,45–54] In addition, the rate performance of V_2O_5//Zn and V_2O_5//Zn@SiO_2-SA is also evaluated (Figure S24, Supporting Information).

The influence of the SiO_2@SA film on the EDL structure is also investigated by theoretical approaches (**Figure 4**). Intermolecular interaction is mainly composed of electrostatic interaction and van der Waals force, and the former generally plays a decisive role in noncovalent interaction for polar molecules or ions. For the interpretation of electrostatic interaction, the molecular electrostatic potential (MESP) V(r) analysis derived from DFT calculations is employed.[55] V(r) in the whole surface region of SA molecule is entirely negative (Figure 4a), which is associated with the lone pair electrons of oxygen atoms in hydroxyl and carboxyl groups. V(r)s of SA

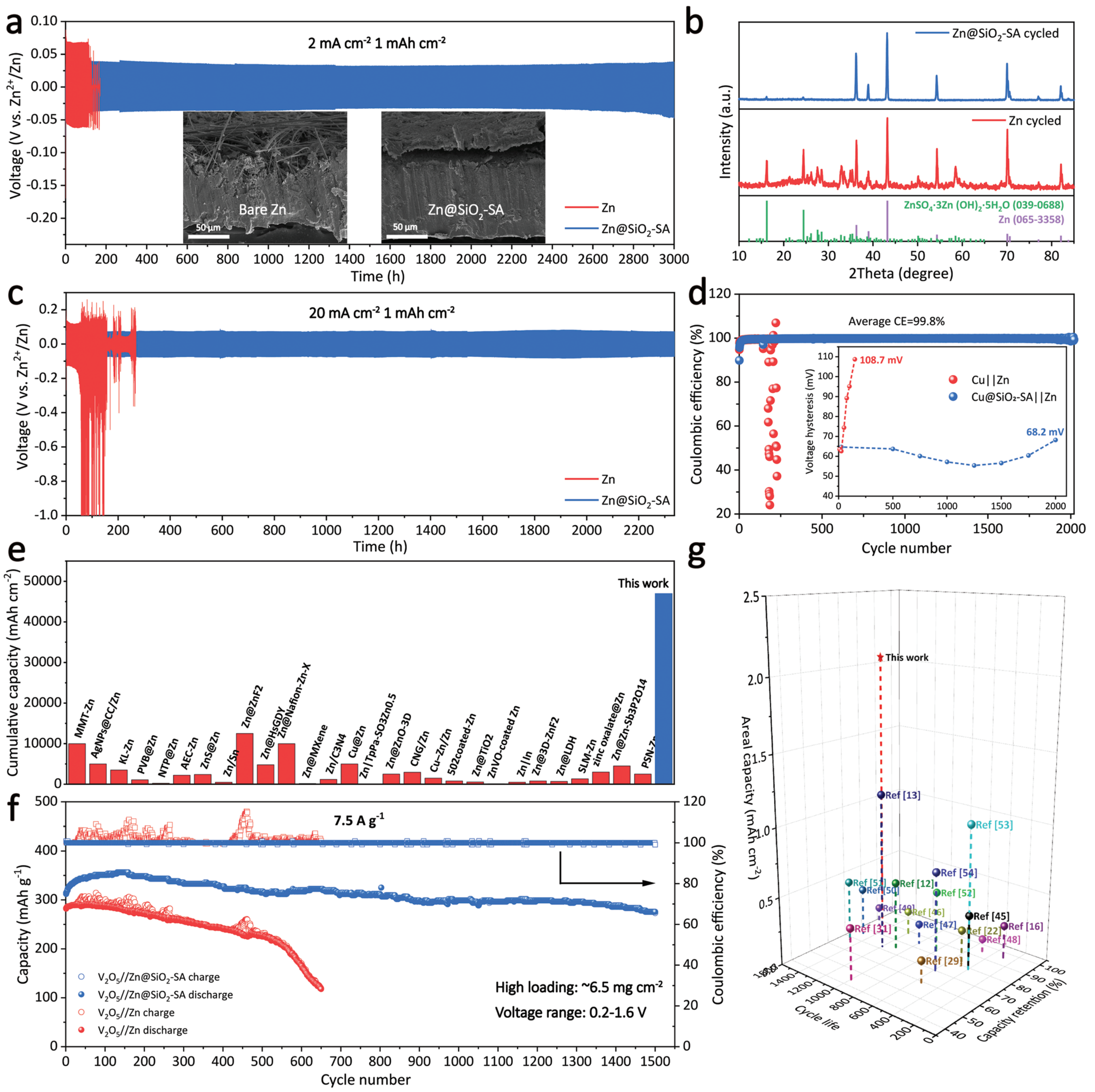

Figure 3. Voltage-time curves for symmetrical cells of bare Zn and Zn@SiO_2-SA electrodes a) at 2 mA cm^{-2} for 1 mAh cm^{-2} (insets are the cross-sectional SEM images of both electrodes after 100 cycles) and c) at 20 mA cm^{-2} for 1 mAh cm^{-2}. b) XRD patterns of bare Zn and Zn@SiO_2-SA electrodes after 100 cycles. d) CEs of Cu||Zn and Cu@SiO_2-SA||Zn half cells at 2 mA cm^{-2} with a fixed deposition capacity of 1 mAh cm^{-2} (insets are corresponding voltage hysteresis). e) Cumulative capacities between the Zn@SiO_2-SA electrode and other recently reported Zn metal anodes based on the interface modification strategy. f) Cycling performances of the high-loading V_2O_5//Zn and V_2O_5//Zn@SiO_2-SA cells between 0.2 and 1.6 V at 7.5 A g^{-1}. g) The comparison of electrochemical performance between the V_2O_5//Zn@SiO_2-SA cell and recently reported Zn metal batteries in terms of areal capacity, cycle life and capacity retention.

and SO_4^{2-} have the same sign and thus lead to electrostatic repulsion. Accordingly, the opposite $V(r)$s of SA and Zn^{2+} give rise to the electrostatic attraction. Besides, one complementary region of $V(r)$ is also observed for the interaction between SA and H_2O, revealing the hydrogen bonding nature. Furthermore, the vdW force, possible chemical force and solvation effect are integrally considered in these systems to quantify various interaction energies (Figure 4b). As the species of Zn^{2+} and H_2O approach SA gradually, there are apparent potential wells of −1.61 and −0.36 eV, respectively, which indicates the good coordination environment surrounding SA chains. The net potential energy between SO_4^{2-} and SA is

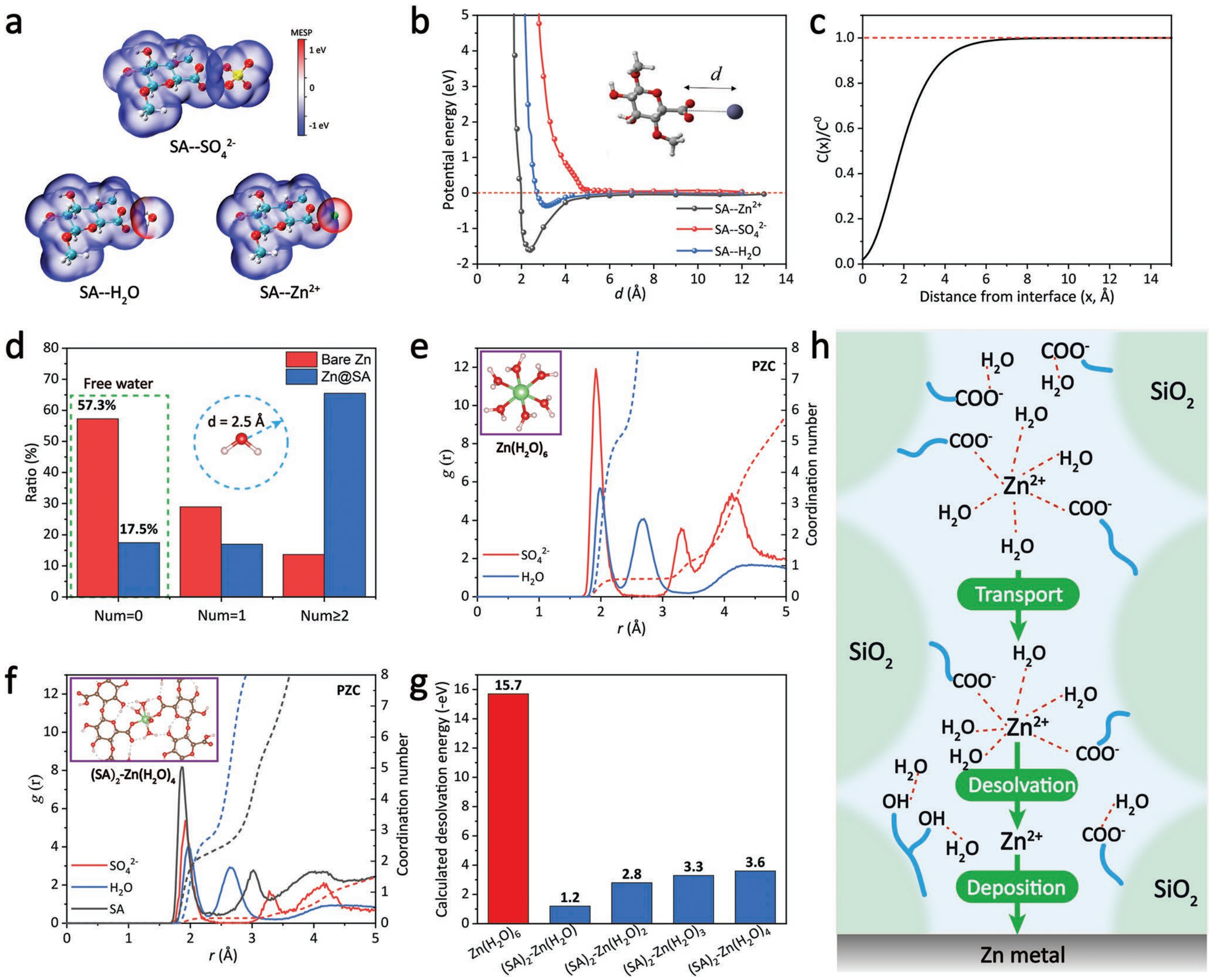

Figure 4. a) MESP isosurface plots between SA and different species of SO_4^{2-}, H_2O and Zn^{2+}. b) The energy of interaction between different species as a function of their distance obtained from quantum chemistry calculation. c) The calculated SO_4^{2-} distribution near the SiO_2-SA interface. d) The ratio of H_2O with different coordination numbers of non-water molecules in Zn and Zn@SA interfaces at the PZC. RDFs (solid line) and corresponding coordination numbers (dash lines) of Zn^{2+} solvation sheath in e) Zn and f) Zn@SA interfaces at the PZC. g) The calculated desolvation energy barriers in Zn and Zn@SA interfaces. h) Schematic illustration of Zn^{2+} charge-transfer process on the Zn@SiO_2-SA electrode.

positive and increases exponentially as the distance decreases, indicating strong repulsive energy. The altered interaction energy as produced by SA chains affects the distribution and chemical environment of SO_4^{2-}, H_2O and Zn^{2+}. Due to the electrostatic field produced by the SiO_2-SA layer, SO_4^{2-} anions near the SiO_2-SA interface are distributed according to the Boltzmann's law:[56]

$$c(x)/c^0 = \exp\left[-zF\varphi(x)/\mathrm{RT}\right] \tag{1}$$

where x is defined as the distance from the SiO_2-SA/electrolyte interface to SO_4^{2-}, c^0 is the concentration of SO_4^{2-} in the bulk electrolyte, z is the charge number of SO_4^{2-}, and F is the Faraday's constant. φ(x) is expressed by the Poisson equation:

$$\varphi(\mathrm{x}) = \varphi_0 \exp(-k\mathrm{x}) \tag{2}$$

where φ_0 is the potential at the equipotential surface, which is the zeta potential of SiO_2-SA surface (–50.18 mV, Figure S25, Supporting Information) and $1/k$ is the Debye length, as depicted with the following equation:

$$1/k = \left(2z^2F^2c^0/\varepsilon RT\right)^{-1/2} \tag{3}$$

where ε is the dielectric constant of solvent, R is the gas constant, and T is the absolute temperature. The distribution of SO_4^{2-} at the position (x) is therefore calculated as:

$$c(x)/c^0 = \exp\left[\left(-zF/RT\right)\varphi_0 \exp\left[-\mathrm{x}\left(2z^2F^2c^0/\varepsilon RT\right)^{1/2}\right]\right] \tag{4}$$

As depicted in Figure 4c, the local concentration of SO_4^{2-} decreases significantly with the reduced distance. As x is close to zero, there is almost no SO_4^{2-} and, thus, the penetration of SO_4^{2-} toward Zn metal surface is effectively prevented.

Next, we examine the coordination number of H_2O with non-water molecules in EDLs of Zn and Zn@SA interfaces through MD simulation results by counting the number of coordinating species within the distance of 2.5 Å from H_2O molecules. Figure 4d shows that the ratio of free water in Zn@SA interface (17.5%) is much below that in Zn interface (57.3%) at the PZC. Moreover, the ratio of H_2O with high coordination numbers (≥2) for the Zn@SA interface (65.5%) is dominated due to the favorable interaction between SA and H_2O. Similar comparison results are also observed at the plating/stripping potentials (Figure S26, Supporting Information). The reduction of free water in the Zn@SiO_2-SA electrode interface is beneficial for constraining HER confirmed by linear sweep voltammetry curves (Figure S27, Supporting Information) and pounch cell tests (Figure S28, Supporting Information).

Radial distribution functions (RDFs) obtained from MD simulations are applied to analyze the first Zn^{2+} solvation sheath in both EDLs. The coordination numbers of H_2O and SO_4^{2-} in the bare Zn interface at the PZC are ≈5.5 and 0.5, respectively, as consistent with the previously reported solvation structure of Zn^{2+} $(H_2O)_6$ (Figure 4e). For the Zn@SA interface, SO_4^{2-} is barely detected in the solvation shell, and SA is involved to replace H_2O due to the preferred interaction between SA and Zn^{2+}. The coordination numbers of SA and H_2O are estimated to be ≈2.5 and 3.5, respectively (Figure 4f). The similar conclusion is also deduced at the potentials of −40 mV and +100 mV (Figure S29, Supporting Information). Since the desolvation process is generally accepted to be the rate-determining step during Zn deposition, the desolvation energy is also calculated by DFT based on the reliable solvation structures (Figure 4g).[21] For bare Zn, the H_2O shell must be removed at the OHL prior to Zn deposition ($Zn^{2+} (H_2O)_6 \rightarrow Zn^{2+} + 6H_2O$), resulting in a large desolvation energy barrier of 15.7 eV. In comparison, the desolvation process with SA is significantly promoted due to the existence of this complex structure ($(SA)_2 - Zn^{2+} (H_2O)_x \rightarrow (SA)_2 - Zn^{2+} + xH_2O$). Furthermore, the desolvation energy barrier is reduced gradually with fewer H_2O molecules (x), which is as low as 1.2 eV for the coordinating environment of $(SA)_2 - Zn^{2+} (H_2O)$. In addition to theoretical calculations, various experimental characterizations are also conducted to examine the ionic speciation differences of the electrochemical interface. As depicted in the Raman spectra (Figure S30, Supporting Information), the ratio of the peak intensity of SO_4^{2-} to that of H_2O [$I(SO_4^{2-})/I(H_2O)$] for the Zn@SA interface (0.49) and Zn@SiO_2-SA interface (0.28) are significantly lower than that of the Zn interface (3.64), implying the similar charge repulsion effect of SA and SiO_2-SA layers. Moreover, the more precise ratio of Zn^{2+} and SO_4^{2-} concentration in the SA layer of Zn@SA electrode is ≈2.61 by inductively coupled plasma-optical emission spectrometry (ICP-OES) and ion chromatography (IC), which is larger than that in the bulk electrolyte with the standard concentration ratio of 1. Differential capacitance curves (Figure S31a, Supporting Information) show that the surface capacitance of bare Ti (20.1 μF cm^{-2}) is much larger than those of Ti@SA interface (9.9 μF cm^{-2}) and the Ti@SiO_2-SA interface (12.8 μF cm^{-2}) at the PZC (−0.48 V vs Ag/AgCl), implying the higher content of H_2O and SO_4^{2-} anions in the EDL without SA. Cs in the EDL of Ti@SA and Ti@SiO_2-SA interfaces remain unchanged during the linear sweep voltammetry, reflecting the relatively stable EDL structure through the introduction of SA. Compared with pure H_2O, de-shielding in ^1H NMR (from H_2O) is observed in 2 M $ZnSO_4$ solution due to the strong coordination between Zn^{2+} and H_2O with the solvation structure of Zn^{2+} $(H_2O)_6$ (Figure S31b, Supporting Information). However, the de-shielding effect is weakened with the addition of 2.5 wt.% SA due to the preferential coordination of Zn^{2+} with negatively charged SA molecules, corroborating the regulated solvation structure of $(SA)_2 - Zn^{2+} (H_2O)_x$ through MD simulations.

The complete Zn^{2+} charge-transfer mechanism on the Zn@SiO_2-SA electrode is illustrated in Figure 4h. In the SiO_2-SA layer, uniformly packed SiO_2 nanoparticles create an integrated framework. SA polymer chains are firmly tied to the surface of SiO_2 through the hydrogen bonds between -OH and Si-O groups, serving as fast Zn^{2+} migration channels. In such systems, Zn^{2+} ions form coordination bonds with carboxylic oxygen of SA chains, which can move from one site to another in the presence of an electric field. Moreover, the diffusion energy barrier of Zn^{2+} along SA polymer chains is estimated to be ≈0.71 eV (Figure S32, Supporting Information), which is even comparable to the values of Zn^{2+}-conductive layered materials.[57–61] The apparent Zn^{2+} transport ability is further enhanced through the polymer chain conformational transformation caused by segmental motion and H_2O molecules.[62] As the anions are fixed to the polymer, most transport species are Zn^{2+} cations, so the improved $t_{Zn^{2+}}$ is reasonable. As solvated Zn^{2+} ions approach the electrode surface, H_2O is removed from the solvation sheath of $(SA)_2 - Zn^{2+}$ $(H_2O)_x$ to release Zn^{2+}, leading to the uniform Zn deposition behavior.

To further verify the effectiveness of our proposed EDL configuration strategy, the capability of regulating EDL based on other polyanionic polysaccharide polymers is examined with both experimental and theoretical routes. Similar to the molecule structure of SA, poly anionic cellulose (PAC) and K-carrageenan (CGN) also contain abundant hydroxyl groups (Figure S33, Supporting Information). Furthermore, carboxylic groups in PAC and sulfonate group in CGN give rise to negative V(r) analogous to that of SA (Figure S34a,c, Supporting Information), which leads to not only the electrostatic repulsion between SO_4^{2-} and polymer molecules but also the coordination between H_2O, Zn^{2+} and polymer molecules (Figure S34b,d, Supporting Information). Accordingly, SO_4^{2-} anions for Zn@PAC and Zn@CGN interfaces at various potentials are calculated to be excluded in the EDL (Figures S35 and S36, Supporting Information). In addition, the symmetrical cells of Zn@SiO_2-PAC and Zn@SiO_2-CGN electrodes and half cells of Cu@SiO_2-PAC and Cu@SiO_2-CGN electrodes also deliver improved cycling stability and enhanced CE as compared with bare Zn (Figures S37 and S38, Supporting Information), demonstrating that the configuration of EDL structure can also be realized by using other polyanionic polysaccharide polymers, showing its great potential as a universal modulation strategy of Zn metal anodes.

3. Conclusions

In this work, a SiO_2-sodium alginate organic/inorganic hybrid film is proposed to reconfigure the inner Helmholtz layer for Zn metal anodes. The robust and elastic organic/inorganic hybrid film provides sufficient mechanical rigidity to suppress the growth of Zn dendrites. The high electrostatic repulsive force produced by SA enables the SiO_2-SA film to serve as an appropriate screening layer to prevent the permeation of SO_4^{2-} anions into the EDL. Moreover, free water is also substantially reduced through hydrogen bond interaction. Abundant carboxylic groups in the EDL are beneficial to regulating the coordination environment of solvated Zn^{2+}, minimizing the desolvation penalties. These synergetic effects contribute to excellent cycling stability of the Zn@SiO_2-SA electrode under extreme conditions (e.g., a long lifespan of 2350 h at 20 mA cm^{-2}). Notably, the high-loading V_2O_5//Zn@SiO_2-SA zinc metal full battery achieves a high areal capacity of 2.05 mAh cm^{-2} with an average capacity decay rate of only 0.0079% per cycle. Regarding the simplicity and scalability of the preparation method, the EDL configuration strategy is expected to provide new opportunities for developing AZMBs for practical applications.

Supporting Information

Supporting Information is available from the Wiley Online Library or from the author.

Acknowledgements

Y.Y. and H.M.H. contributed equally to this work. This work was supported by National Natural Science Foundation of China (22109030), the Key Research and Development Program of Yunnan Province (202103AA080019), Fujian Industrial Technology Development and Application Plan (2022I0002) and Guangdong Province Basic and Applied Basic Research Fund (2019A1515111069 and 2021A1515010177). The theoretical calculation was supported by Open Research Fund of CNMGE Platform & NSCC-TJ. The authors thank Prof. Jinchao Dong and Mr. Fan Gao at Xiamen University for their help in the Raman tests. The authors also thank Mr. Pengxiang Lin and Mr. Dongzheng Wu at Xiamen University for their help in the measurements of differential capacitance curves and ^{1}H NMR.

Conflict of Interest

The authors declare no conflict of interest.

Data Availability Statement

The data that support the findings of this study are available from the corresponding author upon reasonable request.

Keywords

aqueous zinc metal batteries, charge repulsion, electric double layers, molecular dynamics, zinc anodes

Received: October 26, 2022
Revised: November 28, 2022
Published online:

[1] D. Chao, W. Zhou, F. Xie, C. Ye, H. Li, M. Jaroniec, S.-Z. Qiao, *Sci. Adv.* **2020**, *6*, eaba4098.
[2] Y. Zhao, Z. Chen, F. Mo, D. Wang, Y. Guo, Z. Liu, X. Li, Q. Li, G. Liang, C. Zhi, *Adv. Sci.* **2021**, *8*, 2002590.
[3] J. Zheng, Q. Zhao, T. Tang, J. Yin, C. D. Quilty, G. D. Renderos, X. Liu, Y. Deng, L. Wang, D. C. Bock, C. Jaye, D. Zhang, E. S. Takeuchi, K. J. Takeuchi, A. C. Marschilok, L. A. Archer, *Science* **2019**, *366*, 645.
[4] Q. Yang, Q. Li, Z. Liu, D. Wang, Y. Guo, X. Li, Y. Tang, H. Li, B. Dong, C. Zhi, *Adv. Mater.* **2020**, *32*, 2001854.
[5] Z. Cao, P. Zhuang, X. Zhang, M. Ye, J. Shen, P. M. Ajayan, *Adv. Energy Mater.* **2020**, *10*, 2001599.
[6] H. Yang, Y. Qiao, Z. Chang, H. Deng, X. Zhu, R. Zhu, Z. Xiong, P. He, H. Zhou, *Adv. Mater.* **2021**, *33*, 2102415.
[7] F. Wang, O. Borodin, T. Gao, X. Fan, W. Sun, F. Han, A. Faraone, J. A. Dura, K. Xu, C. Wang, *Nat. Mater.* **2018**, *17*, 543.
[8] X. Wu, Y. Xu, C. Zhang, D. P. Leonard, A. Markir, J. Lu, X. Ji, *J. Am. Chem. Soc.* **2019**, *141*, 6338.
[9] J. Zhao, J. Zhang, W. Yang, B. Chen, Z. Zhao, H. Qiu, S. Dong, X. Zhou, G. Cui, L. Chen, *Nano Energy* **2019**, *57*, 625.
[10] L. Cao, D. Li, E. Hu, J. Xu, T. Deng, L. Ma, Y. Wang, X.-Q. Yang, C. Wang, *J. Am. Chem. Soc.* **2020**, *142*, 21404.
[11] W. Yang, X. Du, J. Zhao, Z. Chen, J. Li, J. Xie, Y. Zhang, Z. Cui, Q. Kong, Z. Zhao, C. Wang, Q. Zhang, G. Cui, *Joule* **2020**, *4*, 1557.
[12] H. Yan, S. Li, Y. Nan, S. Yang, B. Li, *Adv. Energy Mater.* **2021**, *11*, 2100186.
[13] T. Chen, Y. Wang, Y. Yang, F. Huang, M. Zhu, B. T. W. Ang, J. M. Xue, *Adv. Funct. Mater.* **2021**, *31*, 2101607.
[14] C. Deng, X. Xie, J. Han, Y. Tang, J. Gao, C. Liu, X. Shi, J. Zhou, S. Liang, *Adv. Funct. Mater.* **2020**, *30*, 2000599.
[15] M. Liu, J. Cai, H. Ao, Z. Hou, Y. Zhu, Y. Qian, *Adv. Funct. Mater.* **2020**, *30*, 2004885.
[16] R. Zhao, Y. Yang, G. Liu, R. Zhu, J. Huang, Z. Chen, Z. Gao, X. Chen, L. Qie, *Adv. Funct. Mater.* **2020**, *31*, 2001867.
[17] J. Hao, B. Li, X. Li, X. Zeng, S. Zhang, F. Yang, S. Liu, D. Li, C. Wu, Z. Guo, *Adv. Mater.* **2020**, *32*, 2003021.
[18] S. Li, J. Fu, G. Miao, S. Wang, W. Zhao, Z. Wu, Y. Zhang, X. Yang, *Adv. Mater.* **2021**, *33*, 2008424.
[19] L. Ma, Q. Li, Y. Ying, F. Ma, S. Chen, Y. Li, H. Huang, C. Zhi, *Adv. Mater.* **2021**, *33*, 2007406.
[20] Q. Yang, Y. Guo, B. Yan, C. Wang, Z. Liu, Z. Huang, Y. Wang, Y. Li, H. Li, L. Song, J. Fan, C. Zhi, *Adv. Mater.* **2020**, *32*, 2001755.
[21] Y. Cui, Q. Zhao, X. Wu, X. Chen, J. Yang, Y. Wang, R. Qin, S. Ding, Y. Song, J. Wu, K. Yang, Z. Wang, Z. Mei, Z. Song, H. Wu, Z. Jiang, G. Qian, L. Yang, F. Pan, *Angew. Chem.* **2020**, *59*, 16594.
[22] N. Zhang, S. Huang, Z. Yuan, J. Zhu, Z. Zhao, Z. Niu, *Angew. Chem.* **2020**, *60*, 2861.
[23] P. Liu, Z. Zhang, R. Hao, Y. Huang, W. Liu, Y. Tan, P. Li, J. Yan, K. Liu, *Chem. Eng. J.* **2021**, *403*, 126425.
[24] Y. Zhang, G. Wang, F. Yu, G. Xu, Z. Li, M. Zhu, Z. Yue, M. Wu, H.-K. Liu, S.-X. Dou, C. Wu, *Chem. Eng. J.* **2021**, *416*, 128062.
[25] S. Park, *Chem. Sci.* **2020**, *11*, 11692.
[26] X. Xie, S. Liang, J. Gao, S. Guo, J. Guo, C. Wang, G. Xu, X. Wu, G. Chen, J. Zhou, *Energy Environ. Sci.* **2020**, *13*, 503.
[27] X. Zhang, J. Li, D. Liu, M. Liu, T. Zhou, K. Qi, L. Shi, Y. Zhu, Y. Qian, *Energy Environ. Sci.* **2021**, *14*, 3120.
[28] Z. Cai, Y. Ou, J. Wang, R. Xiao, L. Fu, Z. Yuan, R. Zhan, Y. Sun, *Energy Storage Mater.* **2020**, *27*, 205.
[29] Z. Cao, X. Zhu, D. Xu, P. Dong, M. O. L. Chee, X. Li, K. Zhu, M. Ye, J. Shen, *Energy Storage Mater.* **2021**, *36*, 132.
[30] Q. Zhang, J. Luan, X. Huang, Q. Wang, D. Sun, Y. Tang, X. Ji, H. Wang, *Nat. Comm.* **2020**, *11*, 3961.
[31] P. Xiao, L. Xue, Y. Guo, L. Hu, C. Cui, H. Li, T. Zhai, *Sci. Bull.* **2021**, *66*, 545.

[32] D. Han, S. Wu, S. Zhang, Y. Deng, C. Cui, L. Zhang, Y. Long, H. Li, Y. Tao, Z. Weng, Q. H. Yang, F Kang, *Small* **2020**, *16*, 2001736.
[33] Y. Yang, C. Liu, Z. Lv, H. Yang, Y. Zhang, M. Ye, L. Chen, J. Zhao, C. C. Li, *Adv. Mater.* **2021**, *33*, 2007388.
[34] Y. Yang, C. Liu, Z. Lv, H. Yang, X. Cheng, S. Zhang, M. Ye, Y. Zhang, L. Chen, J. Zhao, C. C. Li, *Energy Storage Mater.* **2021**, *41*, 230.
[35] X. Wang, J. Meng, X. Lin, Y. Yang, S. Zhou, Y. Wang, A. Pan, *Adv. Funct. Mater.* **2021**, *31*, 2106114.
[36] S. Wu, S. Zhang, Y. Chu, Z. Hu, J. Luo, *Adv. Funct. Mater.* **2021**, *31*, 2107397.
[37] S. Zhou, Y. Wang, H. Lu, Y. Zhang, C. Fu, I. Usman, Z. Liu, M. Feng, G. Fang, X. Cao, S. Liang, A. Pan, *Adv. Funct. Mater.* **2021**, *31*, 2104361.
[38] Y. Zhang, M. Zhu, G. Wang, F. H. Du, F. Yu, K. Wu, M. Wu, S. X. Dou, H. K. Liu, C. Wu, *Small Methods* **2021**, *5*, 2100650.
[39] C. Huang, X. Zhao, S. Liu, Y. Hao, Q. Tang, A. Hu, Z. Liu, X. Chen, *Adv. Mater.* **2021**, *33*, 2100445.
[40] H. Li, S. Wei, C. Qing, J. Yang, *J. Colloid Interface Sci.* **2003**, *258*, 40.
[41] W. Sun, F. Wang, B. Zhang, M. Zhang, V. Küpers, X. Ji, C. Theile, P. Bieker, K. Xu, C. Wang, M. Winter, *Science* **2021**, *371*, 46.
[42] C. Yan, H.-R. Li, X. Chen, X.-Q. Zhang, X.-B. Cheng, R. Xu, J.-Q. Huang, Q. Zhang, *J. Am. Chem. Soc.* **2019**, *141*, 9422.
[43] H. Yan, S. Li, H. Xu, H. Chen, S. Yang, B. Li, *Adv. Energy Mater.* **2022**, *12*, 2201599.
[44] H. Yan, C. Han, S. Li, J. Liu, J. Ren, S. Yang, B. Li, *Chem. Eng. J.* **2022**, *442*, 136081.
[45] Y. Lu, T. Zhu, N. Xu, K Huang, *ACS Appl Energy Mater* **2019**, *2*, 6904.
[46] B. W. Olbasa, F. W. Fenta, S.-F. Chiu, M.-C. Tsai, C.-J. Huang, B. A. Jote, T. T. Beyene, Y.-F. Liao, C.-H. Wang, W.-N. Su, H. Dai, B. J. Hwang, *ACS Appl. Energy Mater.* **2020**, *3*, 4499.
[47] J. Ding, Y. Liu, S. Huang, X. Wang, J. Yang, L. Wang, M. Xue, X. Zhang, J. Chen, *ACS Appl. Mater. Interfaces* **2021**, *13*, 29746.
[48] Y. An, Y. Tian, S. Xiong, J. Feng, Y Qian, *ACS Nano* **2021**, *15*, 11828.
[49] J. Hao, X. Li, S. Zhang, F. Yang, X. Zeng, S. Zhang, G. Bo, C. Wang, Z. Guo, *Adv. Funct. Mater.* **2020**, *30*, 2001263.
[50] R. Xiao, Z. Cai, R. Zhan, J. Wang, Y. Ou, Z. Yuan, L. Wang, Z. Lu, Y. Sun, *Chem. Eng. J.* **2021**, *420*, 129642.
[51] J. Shi, K. Xia, L. Liu, C. Liu, Q. Zhang, L. Li, X. Zhou, J. Liang, Z. Tao, *Electrochim. Acta* **2020**, *358*, 136937.
[52] H. He, J. Liu, *J. Mater. Chem. A* **2020**, *8*, 22100.
[53] P. Xu, C. Wang, B. Zhao, Y. Zhou, H. Cheng, *J. Colloid Interface Sci.* **2021**, *602*, 859.
[54] J. Cui, Z. Li, A. Xu, J. Li, M Shao, *Small* **2021**, *17*, 2100722.
[55] J. S. Murray, P. Politzer, *WIREs Comput. Mol. Sci.* **2011**, *1*, 153.
[56] O. M. B. John, A. K. N. Reddy, M. Gamboa-Aldeco, *Modern Electrochemistry*, Kluwer Academic Publishers, Dordrecht, Netherlands **2002**.
[57] Z. Li, Y. Ren, L. Mo, C. Liu, K. Hsu, Y. Ding, X. Zhang, X. Li, L. Hu, D. Ji, G Cao, *ACS Nano* **2020**, *14*, 5581.
[58] W. Li, K. Wang, S. Cheng, K. Jiang, *Adv. Energy Mater.* **2019**, *9*, 1900993.
[59] T. Wu, K. Zhu, C. Qin, K. Huang, *J. Mater. Chem. A* **2019**, *7*, 5612.
[60] X. Yang, W. Deng, M. Chen, Y. Wang, C.-F. Sun, *Adv. Mater.* **2020**, *32*, 2003592.
[61] Z. Wu, C. Lu, Y. Wang, L. Zhang, L. Jiang, W. Tian, C. Cai, Q. Gu, Z. Sun, L Hu, *Small* **2020**, *16*, 2000698.
[62] I. Nicotera, C. Simari, M. Agostini, A. Enotiadis, S. Brutti, *J. Phys. Chem. C* **2019**, *123*, 27406.